

Article

Metal-Insulator-Metal Waveguide-Based Racetrack Integrated Circular Cavity for Refractive Index Sensing Application

Muhammad A. Butt ^{1,2,*} , Andrzej Kaźmierczak ², Nikolay L. Kazanskiy ^{1,3}  and Svetlana N. Khonina ^{1,3} 

¹ Samara National Research University, 443086 Samara, Russia; kazanskiy@ipsiras.ru (N.L.K.); khonina@ipsiras.ru (S.N.K.)

² Warsaw University of Technology, Institute of Microelectronics and Optoelectronics, Koszykowa 75, 00-662 Warszawa, Poland; andrzej.kazmierczak@pw.edu.pl

³ Institute of RAS-Branch of the FSRC “Crystallography and Photonics” RAS, 443001 Samara, Russia

* Correspondence: butt.m@ssau.ru

Abstract: Herein, a novel cavity design of racetrack integrated circular cavity established on metal-insulator-metal (MIM) waveguide is suggested for refractive index sensing application. Over the past few years, we have witnessed several unique cavity designs to improve the sensing performance of the plasmonic sensors created on the MIM waveguide. The optimized cavity design can provide the best sensing performance. In this work, we have numerically analyzed the device design by utilizing the finite element method (FEM). The small variations in the geometric parameter of the device can bring a significant shift in the sensitivity and the figure of merit (*FOM*) of the device. The best sensitivity and *FOM* of the anticipated device are 1400 nm/RIU and ~12.01, respectively. We believe that the sensor design analyzed in this work can be utilized in the on-chip detection of biochemical analytes.



check for updates

Citation: Butt, M.A.; Kaźmierczak, A.; Kazanskiy, N.L.; Khonina, S.N. Metal-Insulator-Metal Waveguide-Based Racetrack Integrated Circular Cavity for Refractive Index Sensing Application. *Electronics* **2021**, *10*, 1419. <https://doi.org/10.3390/electronics10121419>

Academic Editor: Soo-Jin Kim

Received: 24 May 2021
Accepted: 9 June 2021
Published: 12 June 2021

Publisher's Note: MDPI stays neutral with regard to jurisdictional claims in published maps and institutional affiliations.



Copyright: © 2021 by the authors. Licensee MDPI, Basel, Switzerland. This article is an open access article distributed under the terms and conditions of the Creative Commons Attribution (CC BY) license (<https://creativecommons.org/licenses/by/4.0/>).

Keywords: plasmonics; metal-insulator-metal waveguide; refractive index sensor; biosensing

1. Introduction

Surface plasmon polaritons (hereafter represented as SPPs) are surface electromagnetic (hereafter represented as EM) waves travelling on the metal-dielectric boundary formed by incident photons united with loose electrons [1,2]. The E-field strength of SPPs is tightly constrained with the metal-dielectric border and reduces ominously in the direction perpendicular to the boundary. SPP waves overcome the usual diffraction limit of light and can reach the optical confinement within sub-wavelength order [3]; hence, there are wide-ranging functions of SPP waves [2,3]. However, the sensing devices realized on a SOI platform do not offer high sensitivity [4]. There are several plasmonic waveguide (hereafter represented as WG) structures, for instance, metal-insulator-metal (MIM) [5], insulator-metal-insulator (IMI) [6], metal grooves [7], metal wedge [8], chains of nanoparticles [9], and so on. The MIM WG structure is dominant and offers several extraordinary attributes, such as stronger light confinement, smaller mode size, minimal bending loss, and less costly production expense which has revitalized the implementation of wide-ranging plasmonic devices based on such WG arrangement. Lately, numerous types of MIM WG structure-based plasmonic components are anticipated, such as optical filters [10,11], optical power splitters [12,13], light manipulation [14], and sensing devices [15–18].

Plasmonic sensors based on MIM WG configuration are extensively used for refractive index (hereafter denoted as RI) sensing applications [16,19–24] because of their responsive nature to any slight change in the ambient medium. The main purpose of these exceptional designs is to enhance device performance, such as sensitivity (*S*) and figure of merit (*FOM*). The most widely used performance characteristic of plasmonic sensors is the ability to

identify changes in the RI. The S is calculated in terms of change in resonance wavelength ($\Delta\lambda_{res}$) with respect to the change in ambient refractive index (Δn) and can be written as:

$$S = \frac{\Delta\lambda_{res}}{\Delta n},$$

On the other hand, FOM is expressed as:

$$FOM = \frac{S}{FWHM},$$

where S is the sensitivity of the device and FWHM is the full width at half maximum. This indicates that FWHM plays an important role in maintaining the FOM of the device. In Table 1, we listed several novel sensor designs along with their S and FOM which indicate the importance of unique cavities to enhance the RI sensing capabilities. Recently, two up-to-date review papers on MIM WG-based plasmonic devices have been published and may be consulted for more detailed information (see [25,26]). The researchers anticipated highly attractive sensor designs with unique cavity designs [27–43]. The FOM presented in some reports is very high. It is defined differently in each work and is usually referred to as FOM^* . A high value of FOM is calculated using the expression $\Delta R/(R\Delta n)$ at a fixed wavelength, where ΔR denotes the reflection intensity variation due to Δn of the surrounding medium and R is the reflection rate in the sensor structure. Alternatively, it can also be calculated by utilizing $\Delta T/T\Delta n$, where T denotes the transmittance in the proposed structures and $\Delta T/\Delta n$ is the transmission change at a fixed wavelength induced by a refractive index change.

Table 1. Most recent MIM WG plasmonic sensors based on unique cavity designs.

Ref.	Author	Year	Cavity Shape	S (nm/RIU)	FOM/FOM*
[21]	Butt M.A et al.	2020	NDs loaded square ring	1240	20
[20]	Butt M.A et al.	2020	Multichannel square ring	1948.67	29.52
[24]	Kazanskiy N.L et al.	2020	NDs decorated semi-ring	1084.21	57.06
[30]	Butt M.A et al.	2021	Square ring	1320	16.7
[31]	Qian He et al.	2021	Double half ring	1260	26,000 *
[28]	Chen J et al.	2021	Double symmetric rectangular stubs	1180	5585.3 *
[32]	Rahmatiyar M et al.	2020	Ring resonator	1295	159.6
[27]	Butt M.A et al.	2021	L-shaped cavity	1065	251.17
[33]	Jumat S.Z.B.H et al.	2021	Rectangular and circular resonators including baffles	3400	36
[34]	Rakhshani M.R et al.	2019	Concentric triple racetrack resonators	1618	89
[35]	Sagor R.H et al.	2020	Three quadrilateral cavities	1556	14.83
[36]	Su H et al.	2020	Elliptical ring resonant cavity	1550	43.05
[37]	Zhu J et al.	2020	Key-shaped resonant cavity	1261.67	-
[38]	Chau Y-F. C et al.	2019	T-shape cavity with metal nanorod defects	8280	-
[39]	Butt M.A et al.	2020	Bow Tie configuration	2300	31.5
[40]	Shi H et al.	2021	Racetrack ring resonator	1774	61
[41]	El-Haffar et al.	2020	Elliptical cavity resonator	540	101.3
[42]	Zhang Z et al.	2016	Double rectangular cavities	596	-
[43]	Binfeng Y et al.	2016	Circular cavity resonator	1277	2.1×10^4 *
This work	Butt et al.	2021	Standard racetrack cavity	1200	16.6
This work	Butt et al.	2021	Racetrack integrated circular cavity	1400	12.01

* It is defined differently in each work and is usually referred to as FOM^* .

2. Device Design

In this paper, we propose an attractive and highly sensitive design of a MIM WG RI sensor which is composed of a MIM bus WG coupled to a racetrack integrated circular cavity (hereafter represented as RTICC). Additionally, the device performance is compared with a standard racetrack cavity (hereafter represented as SRTC). The enhancement of the device performance is revealed due to the modification in the cavity design because of improved light-matter interaction. The advantages of the circular [43], rectangular [42], and ellipse [41] cavities are combined in the racetrack cavity. The best choice is to use a circular cavity, but if the radius is too large, the full width at half maximum (FWHM) increases, and the sensing efficiency suffers. The rectangular straight WG is ideal for light propagation, but it can result in a large size at four right angles. The ellipse cavity can enhance the sensing field by providing a strong evanescent field which results in better light-matter interaction. However, its radius of curvature causes significant material loss, so the racetrack cavity is a better alternative.

Gold (Au) is preferred as the metal layer which is deposited on the glass substrate. It is biocompatible and has better endurance to oxidation than silver (Ag). The refractive index of Au is determined from the Drude model:

$$\varepsilon = \varepsilon_{\infty} - \frac{\omega_p^2}{\omega^2 + j\omega\gamma},$$

where $\varepsilon_{\infty} = 9.0685$, $\omega_p = 135.44 \times 10^{14}$ rad/s, and $\gamma = 1.15 \times 10^{14}$ rad/s [44]. In addition, the sensor device is immersed in a dielectric material (denoted as D) of refractive index (n) = 1.3. The width of the bus WG is referred to as W which is fixed at 50 nm. As $W \ll \lambda_{incident}$ therefore, purely TM fundamental mode exists. The distance between the bus WG and the cavity is articulated as g . The radius of the racetrack cavity and the circular cavity is signified as R and R_1 , respectively. The width of the circular cavity is denoted as W_1 . The side length of the racetrack cavity is referred to as L which is fixed at 600 nm. The 2D schematic representation of the SRTC and RTICC design is shown in Figure 1a,b, respectively.

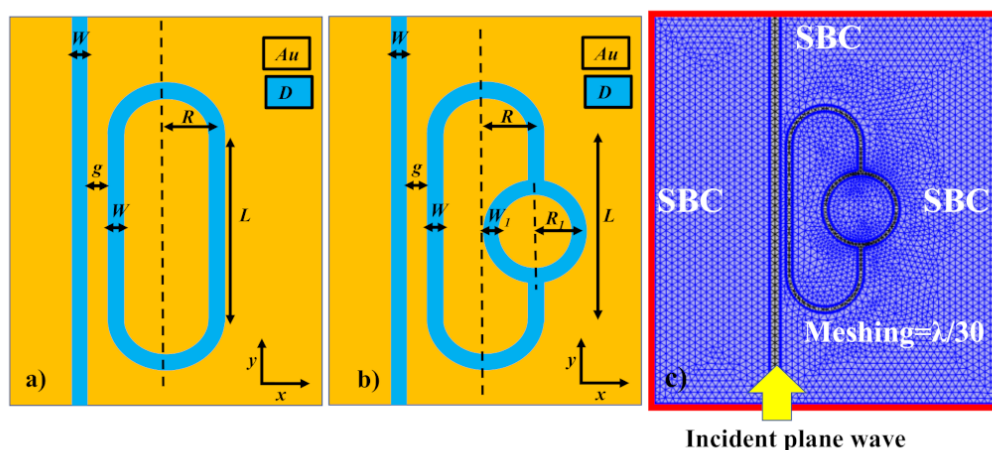


Figure 1. Graphical representation of the MIM WG plasmonic sensor: (a) SRTC, (b) RTICC, (c) meshing of the device design.

The proposed sensor design is adjusted for best sensing efficiency with the help of the 2D finite element method (FEM) by utilizing commercially available COMSOL Multiphysics 5.5 software. The subdomains in the designed device are partitioned into a triangular mesh element with a grid size of $\lambda/30$, to acquire accurate simulation solutions within the existing computational resources as shown in Figure 1c. When resolving the EM wave challenges, it is useful to prototype a domain with open boundaries, that is, a periphery of the computational area across which an EM wave can propagate with no reflection. To

estimate an open geometry, scattering boundary conditions (SBCs) are employed at the outer boundaries of the FEM simulation window. For sensing performance analysis of the plasmonic devices, 2D-FEM is preferred over 3D-FEM because it saves time and requires less computational power as utilized in most of the previous works [19,30,39,45]. However, with the help of the effective index method, the anticipated device height can be calculated.

The cross-sectional model of the MIM WG immersed in water ($n = 1.3$) is shown in Figure 2a. The proposed sensor design can be employed in biomedical applications which is why an ambient medium of $n = 1.3$ is preferred. The real and imaginary effective refractive index (n_{eff}) of the propagating SPP mode at 1000 nm concerning the height (H) and width (w) of the MIM WG is shown in Figure 2b,c, respectively. As H of the MIM WG, or in other words, the Au layer thickness increases, $Re(n_{eff})$ decreases and stabilizes at a certain value of H which indicates the selection of a suitable H of the Au layer. Moreover, the confinement of the SPP mode and the losses associated with the WG can be determined from $Im(n_{eff})$.

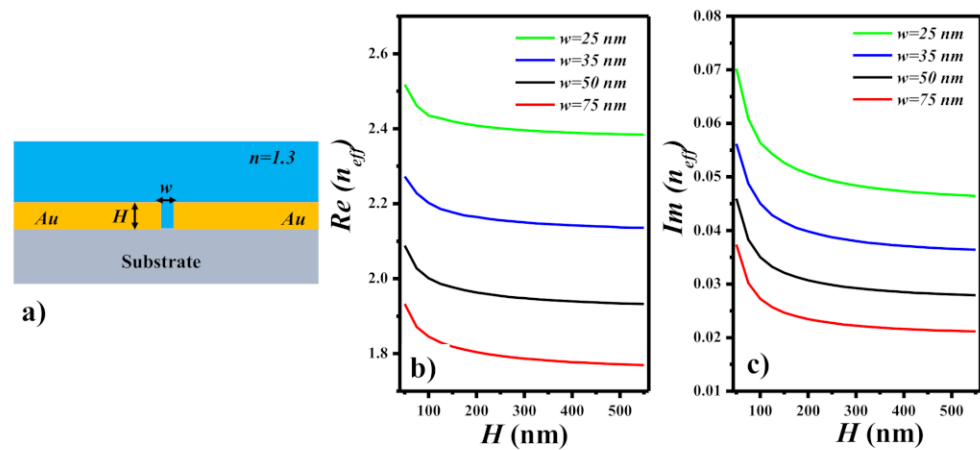


Figure 2. (a) Cross-sectional view of the MIM WG emersed in water ($n = 1.3$). Determination of n_{eff} concerning H and w of the MIM WG: (b) real part, (c) imaginary part.

The $Re(n_{eff})$ decreases from ~ 2.5 to ~ 1.9 as w increases from 25 nm to 75 nm at a constant value of $H = 50$ nm as shown in Figure 2b. This defines the confinement of the SPP mode and its sensitivity to the ambient medium. However, one should choose the appropriate value of w based on the fabrication limit. Moreover, the WG losses reduce as w rises from 25 nm to 75 nm as displayed in Figure 2c. Even if H of the MIM WG approaches infinity, the material losses remain unchanged, which resembles a 2D numerical simulation.

The normalized H-field distribution in the MIM WG at $H = 50$ nm, 200 nm, 400 nm, and 500 nm at the operational wavelength of 1000 nm is shown in Figure 3a–d. Note that w is fixed at 50 nm for all four cases. The SPP TM-fundamental mode is confined in the narrow slot which is exceedingly receptive to the ambient medium. It can be observed that $Re(n_{eff})$ and $Im(n_{eff})$ are inversely related to H of the MIM WG. The $Re(n_{eff}) + Im(n_{eff})$ at $H = 50$ nm is obtained at $2.0888 - 0.045997i$ which reduces to $1.9343 - 0.02807i$ as the H approaches 500 nm and stabilizes at three digits. Therefore, $H > 400$ nm is an appropriate layer thickness of the Au which should be deposited on the glass substrate where $Re(n_{eff})$ is stable and offers low optical losses.

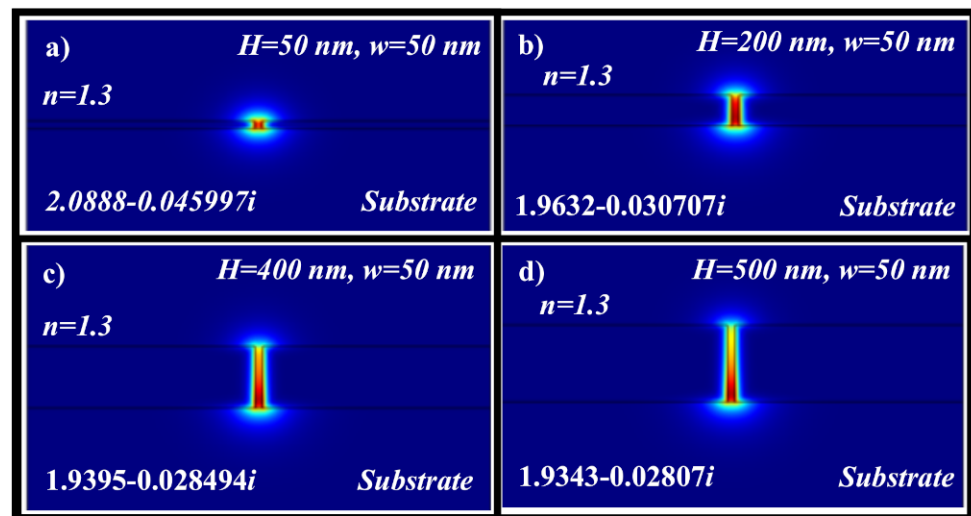


Figure 3. Normalized H-field distribution in the MIM WG at the operation wavelength of 1000 nm: (a) $H = 50$ nm, $w = 50$ nm, (b) $H = 200$ nm, $w = 50$ nm, (c) $H = 400$ nm, $w = 50$ nm, (d) $H = 500$ nm, $w = 50$ nm.

3. SRTC Configuration

To analyze the transmission characteristics of the SRTC configuration, the geometric variables such as R , g , and W of the device design are varied. The analysis is facilitated by the “parametric-sweep” built-in function in COMSOL which allows the calculation of several geometric variables at the same time with no manual external interference. The refractive index of the ambient environment is fixed at 1.3 which will act as a medium for testing the biochemical analytes. From Figure 4a, it can be seen that the R of semi-rings is varied from 170 nm to 210 nm and has a linear control on λ_{res} . The rest of the variables such as W , g , and L are fixed at 50 nm, 20 nm, and 600 nm, respectively. Moreover, the coupling strength of λ_{res} and the FWHM can be optimized by adjusting the gap between the MIM bus WG and the cavity which is denoted as g . The other geometric variables such as W , R , and L are fixed at 50 nm, 180 nm, and 600 nm, respectively. When $g \leq 15$ nm, the FWHM is quite wide, and the coupling strength is low which is not an ideal case. However, the maximum coupling strength and narrow FWHM is obtained at $g = 25$ nm as shown in Figure 4b.

In the last step, the effect of W of the MIM WG on the transmission spectrum is analyzed as shown in Figure 4c. The rest of the geometric variables such as $g = 25$ nm, $R = 180$ nm, and $L = 600$ nm are optimized earlier and employed in this analysis. The value of W is varied between 40 nm and 60 nm. From Figure 4c, it is evident that λ_{res} performs a redshift and increment in coupling strength as W decreases from 60 nm to 40 nm. However, a strong coupling strength comes with a drawback of wide FWHM. Therefore, it is a bargain between a strong resonance dip and a narrow FWHM. Nevertheless, in a practical scenario, a fabrication error of ± 10 nm can alter the final W of the fabricated sample.

The normalized H-field distribution in the SRTC in XY-plane at the on-resonance and off-resonance states at $\lambda_{\text{res}} = 1366$ nm and $\lambda_{\text{res}} = 1800$ nm is shown in Figure 5a,b, respectively. In addition, the 3D H-field distribution at on-resonance and off-resonance states is also shown in Figure 5c,d, respectively, so that the 2D and 3D H-field distributions of the SPP mode can be visualized at both on-resonance and off-resonance states.

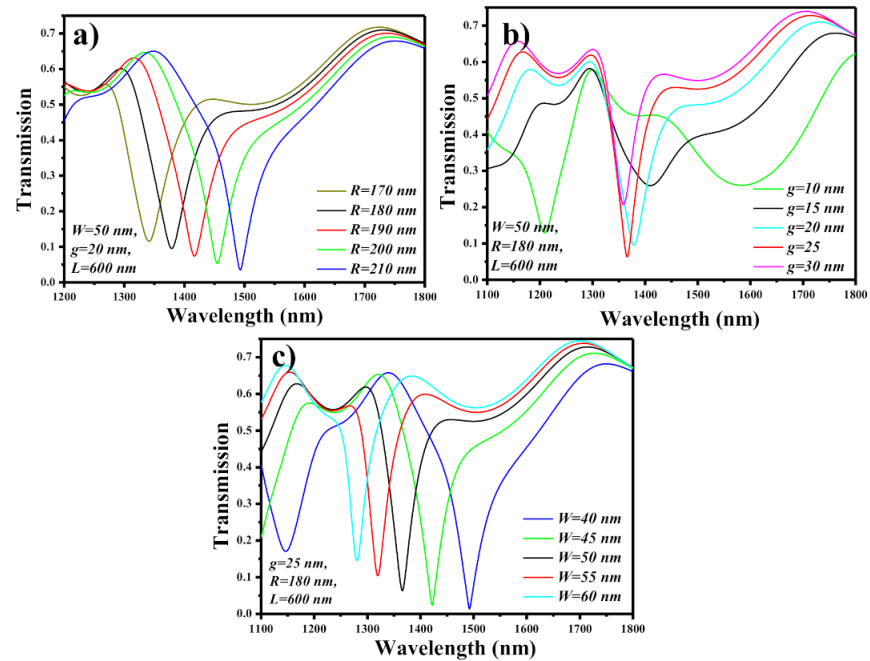


Figure 4. Optimization of standard racetrack cavity: (a) R variation, (b) g variation, (c) W variation.

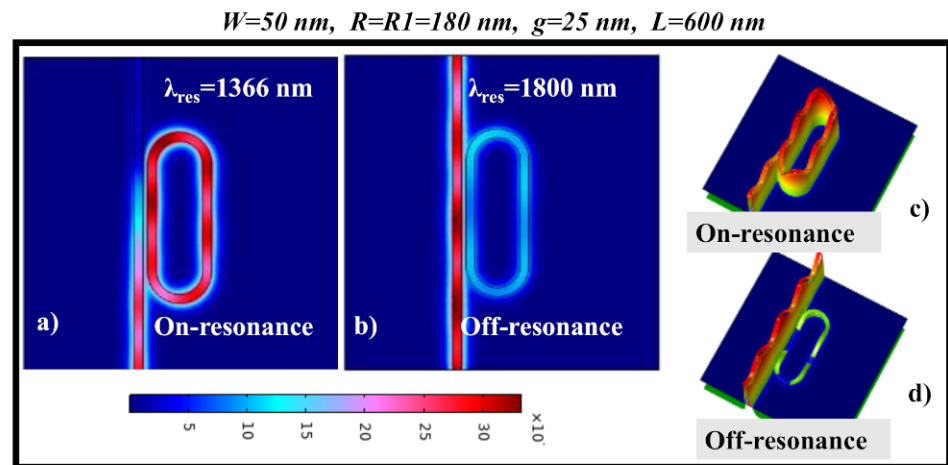


Figure 5. Normalized H-field distribution in the racetrack cavity: (a) on-resonance, (b) off-resonance. 3D-normalized H-field distribution in the racetrack integrated circular cavity: (c) on-resonance, (d) off-resonance.

4. RTICC Configuration

In this section, the geometric variables of the RTICC configuration are optimized for the best sensing performance. Here the following variables such as R , R_1 , W , W_1 , and g are optimized one by one. The transmission spectrum of the RTICC design is plotted for the condition when $R = R_1$ and varied between 170 nm to 210 nm, while the rest of the geometric variables such as g , W , W_1 , and L are fixed at 20 nm, 50 nm, 50 nm, and 600 nm, respectively. Figure 6a shows that λ_{res} dip performs a redshift as R varies from 170 nm to 210 nm. However, at $R \geq 200$ nm, FWHM increases which can deteriorate the FOM of the device. Therefore, we have selected $R = R_1 = 180$ nm as the starting pointing of further investigation. The next step is to choose the appropriate gap (g) between the bus WG and the cavity. The rest of the geometric variables such as W , W_1 , R , R_1 , and L are fixed at 50 nm, 50 nm, 180 nm, 180 nm, and 600 nm, respectively. As a result, the optimum coupling power

is obtained at $g = 20$ nm as shown in Figure 6b. The wide FWHM can be obtained in case $g \leq 15$ nm, which is undesirable.

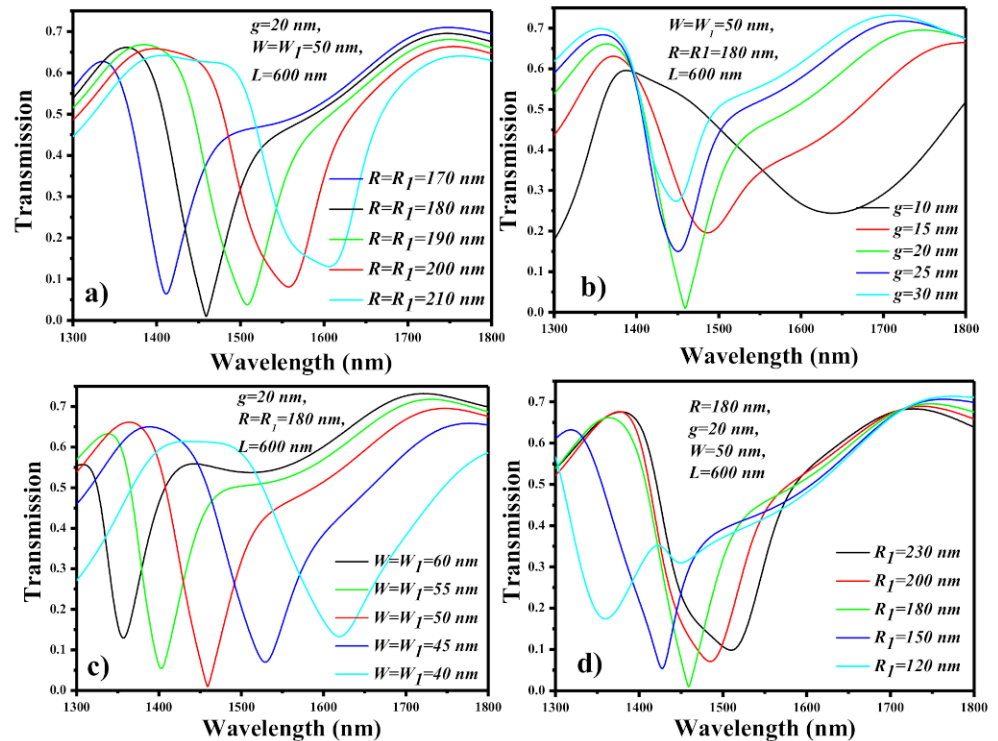


Figure 6. Optimization of racetrack integrated circular cavity: (a) R, R_1 variation (where $R = R_1$), (b) g variation, (c) W, W_1 variation (where $W = W_1$), (d) R_1 variation.

Afterwards the influence of W, W_1 on the transmission spectrum of the RTICC design is analyzed. In this case, $W = W_1$ is considered which is varied between 40 nm and 60 nm. Figure 6c shows that λ_{res} dip performs a blueshift with a reduction in FWHM as W increases from 40 nm to 60 nm. In the end, the influence of $R \neq R_1$ on the transmission spectrum of the RTICC configuration is studied as presented in Figure 6d. The structural variables such as R, g, W, W_1 , and L are fixed at 180 nm, 20 nm, 50 nm, 50 nm, and 600 nm, respectively. In this case, when $R_1 < R$ and $R_1 > R$, the λ_{res} dip performs blueshift and redshift, respectively. Eventually, λ_{res} and FWHM of the sensor can be regulated by several variables individually which signifies large freedom of device optimization.

The normalized H-field distribution in the RTICC in XY-plane at the on-resonance and off-resonance states at $\lambda_{\text{res}} = 1459$ nm and $\lambda_{\text{res}} = 1800$ nm is shown in Figure 7a,b, respectively. In addition, the 3D H-field distribution at on-resonance and off-resonance states is also shown in Figure 7c,d, respectively, so that the 2D and 3D H-field distribution of the SPP mode can be visualized at both on-resonance and off-resonance states.

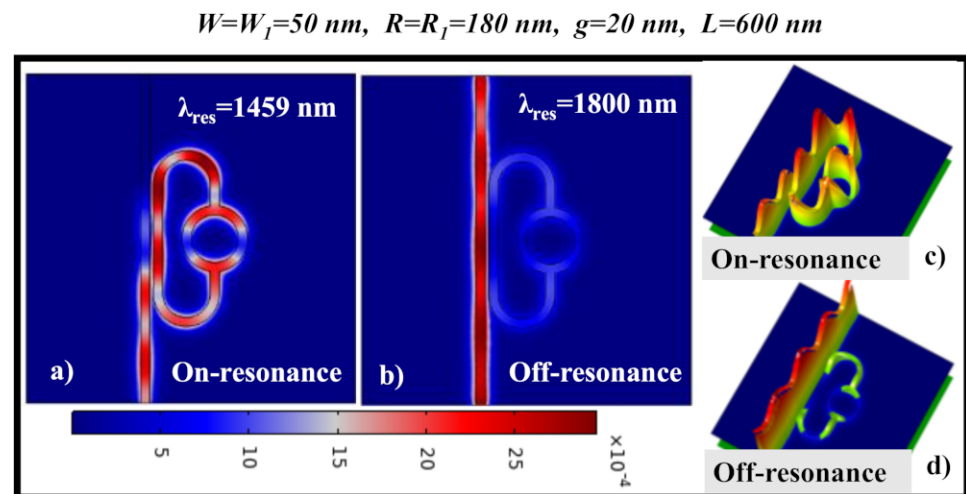


Figure 7. 2D-normalized H-field distribution in the racetrack integrated circular cavity: (a) on-resonance, (b) off-resonance. 3D-normalized H-field distribution in the racetrack integrated circular cavity: (c) on-resonance, (d) off-resonance.

5. Findings and Analysis

SPPs are remarkably receptive to variations in the surrounding RI. Change in RI can be obtained by assessing the deviations in one of the features of the light coupled to the SPP, for example, a shift in the λ_{res} , intensity, or phase. In general, the working principle of the ring resonator or in particular MIM WG plasmonic sensor is established on the wavelength interrogation method which involves the measurement of a shift in λ_{res} relating to the change in the RI of the ambient medium. There are two kinds of wavelength shifts known as redshift and blueshift which can be observed depending on the change (positive or negative) in the RI of the surrounding medium. From other studies [15,27], we learned that by narrowing down the path of the SPP wave by embedding the nano-blocks or nano-walls, the intensity of the SPP wave can be intensified. This leads to the higher light-matter interaction, eventually leading to a higher sensitivity. However, the drawback is wide FWHM which can potentially affect the FOM. Moreover, there are also high chances of $\pm 10\text{ nm}$ of fabrication error which can lead to the variation in the spectral characteristic and device performance. The sensitivity is calculated for the ambient refractive index range of 1.31–1.37. In Table 2, the spectral characteristics and sensing performance of SRTC and RTICC are presented concerning the variation in W and W_1 . The S of SRTC can be enhanced from 1000 nm/RIU to 1200 nm/RIU by reducing W from 50 nm to 30 nm . In the case of RTICC, the S can be varied between 1100 nm/RIU to 1400 nm/RIU by properly regulating W and W_1 . The maximum S and FOM for RTICC is obtained at 1400 nm/RIU and 12.01 for $W = W_1 = 30\text{ nm}$, respectively.

The transmission spectrum of SRTC and RTICC configurations in the presence of different ambient RI values in the range of 1.31 to 1.37 is plotted in Figure 8a,b, respectively. This RI range corresponds to the biological sample analytes. The λ_{res} performs a redshift as the RI of the ambient medium increases from 1.31 to 1.37. However, the amount of shift depends on the sensitivity of the device structure. For a fair analysis, the structural variables such as R and W and W_1 are maintained at 180 nm , 30 nm , and 30 nm , respectively for both designs. The S graph is plotted versus the RIU value of 1.31 to 1.37 for both designs as shown in Figure 8c. Moreover, the S for both designs at each RIU is presented in the table in Figure 8c. The incorporation of a circular cavity in the racetrack cavity provides a better sensing capability as shown in Table 2 and Figure 8c.

Table 2. Spectral characteristics of SRTC and RTICC for $\Delta n = 0.01$.

SRTC	W (nm)	λ_{res} (nm)	FWHM (nm)	S (nm/RIU)	FOM
	30	1637	~72	1200	~16.6
	40	1475	~92	1100	~11.95
	50	1366	~51	1000	~19.6
RTICC	W (nm)/W1 (nm)	λ_{res} (nm)	FWHM (nm)	S (nm/RIU)	FOM
	30/30	1766	~147	1400	~12.01
	40/40	1587	~99	1200	~12.12
	50/50	1459	~80	1100	~13.75
	30/50	1697	~94	1300	~13.8
	30/40	1730	~95	1300	~13.7

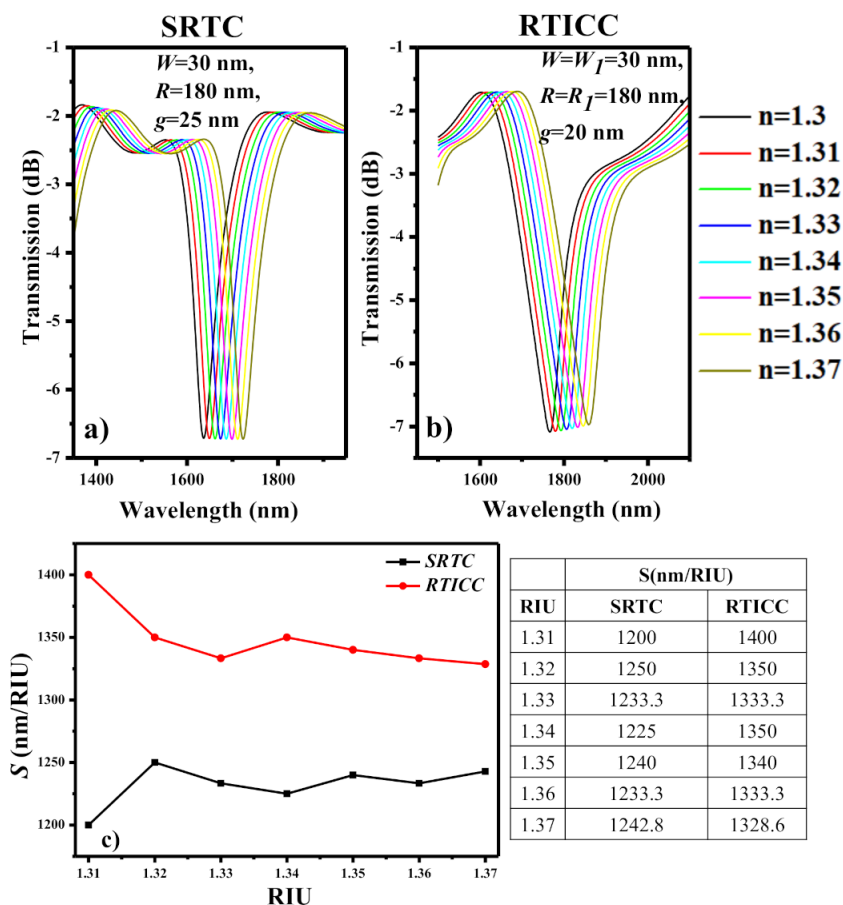


Figure 8. Transmission spectrum versus different ambient RI for (a) SRTC, (b) RTICC, (c) sensitivity versus RIU.

6. Conclusions

In this work, a novel and highly sensitive design of a refractive index sensor based on a metal-insulator-metal (MIM) waveguide is proposed. The sensor design is composed of a racetrack integrated circular cavity side coupled to a MIM bus waveguide. The geometric variables of the device are optimized with the help of the finite element method for the best sensing performance. Moreover, the spectral characteristics and the sensing performance of the proposed sensor design is compared with the standard racetrack cavity design. A significant enhancement in the sensitivity from 1100 nm/RIU to 1400 nm/RIU is obtained

by optimizing the geometric variables of the sensor design. The intended sensor design is an ideal candidate for lab-on-chip biochemical analysis.

Author Contributions: Conceptualization, M.A.B., N.L.K., S.N.K.; methodology, M.A.B., N.L.K., S.N.K.; software, M.A.B., N.L.K., S.N.K.; validation, M.A.B., N.L.K., S.N.K.; formal analysis, M.A.B., N.L.K., S.N.K., A.K.; investigation, M.A.B., N.L.K., S.N.K.; resources, M.A.B., N.L.K., S.N.K.; data curation, M.A.B., N.L.K., S.N.K.; writing—original draft preparation, M.A.B., N.L.K., S.N.K.; writing—review and editing, M.A.B., N.L.K., S.N.K., A.K.; visualization, M.A.B., N.L.K., S.N.K.; supervision, M.A.B., N.L.K., S.N.K.; project administration, M.A.B., N.L.K., S.N.K.; funding acquisition, N.L.K. and S.N.K. All authors have read and agreed to the published version of the manuscript.

Funding: This work was financially supported by the Ministry of Science and Higher Education of the Russian Federation under the Samara National Research University (the scientific state assignment No. 0777-2020-0017) for numerical calculations and under the FSRC “Crystallography and Photonics” of the Russian Academy of Sciences (the state task No. 007-GZ/Ch3363/26) for theoretical research. Additionally, this work was done within the framework of ‘Hybrid sensor platforms of integrated photonic systems based on ceramic and polymer materials’ project is carried out within the TEAM-NET program of the Foundation for Polish Science financed by the European Union under the European Regional Development Fund, POIR.04.04.00-00-14D6/18-01.

Acknowledgments: The authors acknowledge the support provided by the technical staff from Samara National Research University, Russia.

Conflicts of Interest: The authors declare no conflict of interest.

Abbreviations

Standard racetrack cavity	SRTC
Racetrack integrated circular cavity	RTICC
Metal-insulator-metal	MIM
Waveguide	WG
Refractive index	RI
Effective refractive index	n_{eff}
Finite element method	FEM
Sensitivity	S
Figure of merit	FOM

References

1. Anwar, R.S.; Ning, H.; Mao, L. Recent advancements in surface plasmon polaritons-plasmonics in subwavelength structures in microwave and terahertz regimes. *Digit. Commun. Netw.* **2018**, *4*, 244–257. [\[CrossRef\]](#)
2. Zhang, J.; Zhang, L.; Xu, W. Surface plasmon polaritons: Physics and applications. *J. Phys. D Appl. Phys.* **2012**, *45*, 113001. [\[CrossRef\]](#)
3. Zhang, T.; Shan, F. Development and application of surface plasmon polaritons on optical amplification. *Plasmon. Nanophotonics* **2014**, *2014*, 495381. [\[CrossRef\]](#)
4. Karabchevsky, A.; Katiyi, A.; Ang, A.S.; Hazan, A. On-chip nanophotonics and future challenges. *Nanophotonics* **2020**, *9*, 3733–3753. [\[CrossRef\]](#)
5. Zhang, M.; Wang, Z. Analytical method for metal-insulator-metal surface plasmon polaritons waveguide networks. *Opt. Express* **2019**, *27*, 303–321. [\[CrossRef\]](#)
6. Niu, L.; Xiang, Y.; Cai, W.; Zhao, X.; Zhang, N.; Qi, J.; Zhang, X.; Xu, J. Plasmonic Tamm states in insulator-metal-insulator waveguides. *J. Opt. Soc. Am. B* **2018**, *35*, 1368–1373. [\[CrossRef\]](#)
7. Chen, Z.-X.; Wu, Z.-J.; Ming, Y.; Zhang, X.-J.; Lu, Y.-Q. Hybrid plasmonic waveguide in a metal V-groove. *AIP Adv.* **2014**, *4*, 017103. [\[CrossRef\]](#)
8. Feigenbaum, E.; Orenstein, M. Nano plasmon polariton modes of a wedge cross section metal waveguide. *Opt. Express* **2006**, *14*, 8779–8784. [\[CrossRef\]](#) [\[PubMed\]](#)
9. Fevrier, M.; Gogol, P.; Aassaime, A.; Megy, R.; Delacour, C.; Chelnokov, A.; Apuzzo, A.; Blaize, S.; Lourtioz, J.-M.; Dagens, B. Gaint coupling effect between metal nanoparticle chain and optical waveguide. *Nano Lett.* **2012**, *12*, 1032–1037. [\[CrossRef\]](#)
10. Zhai, X.; Liu, Y.; Li, H.; Wujiaihemaiti, R.; Zhu, Y.; Wang, L. Analysis of filter and waveguide effect based on the MIM nanodisk with a metallic block. *J. Nanomater.* **2015**, *2015*, 541409. [\[CrossRef\]](#)
11. Wang, L.; Wang, L.-L.; Zeng, Y.-P.; Xiang, D.; Zhai, X.; Li, X.-F.; Huang, W.-Q. A triangular shaped channel MIM waveguide filter. *J. Mod. Opt.* **2012**, *59*, 1686–1689. [\[CrossRef\]](#)

12. Butt, M.A.; Khonina, S.N.; Kazanskiy, N.L. Ultra-short lossless plasmonic power splitter design based on metal-insulator-metal waveguide. *Laser Phys.* **2019**, *30*, 016201. [[CrossRef](#)]
13. Chen, F.; Xu, Y. Tunable power splitter based on MIM waveguide-rectangular cavity system with Kerr material. *Mod. Phys. Lett. B* **2016**, *30*, 1650376. [[CrossRef](#)]
14. Lu, H.; Wang, G.; Liu, X. Manipulation of light in MIM plasmonic waveguide systems. *Chin. Sci. Bull.* **2013**, *58*, 3607–3616. [[CrossRef](#)]
15. Butt, M.A.; Khonina, S.N.; Kazanskiy, N.L. A multichannel metallic dual nano-wall square split-ring resonator: design analysis and applications. *Laser Phys. Lett.* **2019**, *16*, 126201. [[CrossRef](#)]
16. Butt, M.A.; Khonina, S.N.; Kazanskiy, N.L. A plasmonic colour filter and refractive index sensor applications based on metal-insulator-metal square micro-ring cavities. *Laser Phys.* **2020**, *30*, 016205. [[CrossRef](#)]
17. Mahmud, R.A.; Faruque, M.O.; Sagor, R.H. A highly sensitive plasmonic refractive index sensor based on triangular resonator. *Optics Communications* **2021**, *483*, 126634. [[CrossRef](#)]
18. Khonina, S.N.; Kazanskiy, N.L.; Butt, M.A.; Kazmierczak, A.; Piramidowicz, R. Plasmonic sensor based on metal-insulator-metal waveguide square ring cavity filled with functional material for the detection of CO₂ gas. *Opt. Express* **2021**, *29*, 16584. [[CrossRef](#)]
19. Butt, M.A. Numerical investigation of a small footprint plasmonic Bragg grating structure with a high extinction ratio. *Photonics Lett. Pol.* **2020**, *12*, 82–84. [[CrossRef](#)]
20. Butt, M.A.; Kazanskiy, N.L.; Khonina, S.N. Highly integrated plasmonic sensor design for the simultaneous detection of multiple analytes. *Curr. Appl. Phys.* **2020**, *20*, 1274–1280. [[CrossRef](#)]
21. Butt, M.A.; Khonina, S.N.; Kazanskiy, N.L. An array of nano-dots loaded MIM square ring resonator with enhanced sensitivity at NIR wavelength range. *Optik* **2020**, *202*, 163655. [[CrossRef](#)]
22. Huang, Y.-X.; Xie, Y.-X.; Zhao, W.-L.; Che, H.-J.; Xu, W.-H.; Li, X.; Li, J.-C. A plasmonic refractive index sensor based on a MIM waveguide with a side-coupled nanodisk resonator. In Proceedings of the IEEE 20th International Conference on Embedded and Real-Time Computing Systems and Applications, Chongqing, China, 20–22 August 2014.
23. Kazanskiy, N.L.; Butt, M.A. Enhancing the sensitivity of a standard plasmonic MIM square ring resonator by incorporating nanodots in the cavity. *Photonics Lett. Pol.* **2020**, *12*, 1–3.
24. Kazanskiy, N.L.; Butt, M.A.; Khonina, S.N. Nanodots decorated MIM semi-ring resonator cavity for biochemical sensing applications. *Photonics Nanostruct. Fundam. Appl.* **2020**, *42*, 100836. [[CrossRef](#)]
25. Kazanskiy, N.L.; Butt, M.A.; Degtyarev, S.A.; Khonina, S.N. Achievements in the development of plasmonic waveguide sensors for measuring the refractive index. *Comput. Opt.* **2020**, *44*, 295–318. [[CrossRef](#)]
26. Kazanskiy, N.L.; Khonina, S.N.; Butt, M.A. Plasmonic sensors based on metal-insulator-metal waveguides for refractive index sensing applications: A brief review. *Phys. E Low-Dimens. Syst. Nanostruct.* **2020**, *117*, 113798. [[CrossRef](#)]
27. Butt, M.A.; Kazanskiy, N.L. Nanoblocks embedded in L-shaped nanocavity of a plasmonic sensor for best sensor performance. *Opt. Appl.* **2021**, *51*, 109–120.
28. Chen, J.; Li, J.; Liu, X.; Rohimah, S.; Tian, H.; Qi, D. Fano resonance in a MIM waveguide with double symmetric rectangular stubs and its sensing characteristics. *Opt. Commun.* **2021**, *482*, 126563. [[CrossRef](#)]
29. Yan, S.; Yang, X.; Xu, D.; Su, H.; Wu, X.; Hua, E. MIM structure with inverted M-type cavity for sensing applications. *IEEE Sens. J.* **2021**, *21*, 7468. [[CrossRef](#)]
30. Butt, M.A.; Khonina, S.N.; Kazanskiy, N.L. Metal-insulator-metal nano square ring resonator for gas sensing applications. *Waves Random Complex Media* **2021**, *31*, 146–156. [[CrossRef](#)]
31. He, Q.; Huo, Y.; Guo, Y.; Niu, Q.; Hao, X.; Cui, P.; Wang, Y.; Song, M. Multiple adjustable Fano resonance based on double half ring resonator and its application. *Phys. Scr.* **2021**, *96*, 065504. [[CrossRef](#)]
32. Rahmatiyar, M.; Afsahi, M.; Danaie, M. Design of a refractive index plasmonic sensor based on a ring resonator coupled to a MIM waveguide containing tapered defects. *Plasmonics* **2020**, *15*, 2169–2176. [[CrossRef](#)]
33. Jumat, S.Z.B.H.; Chao, C.-T.C.; Chau, Y.F.C.; Mahadi, A.H.; Kooh, M.R.R.; Kumara, N.T.R.N.; Chiang, H.-P. Plasmonic refractive index sensor based on the combination of rectangular and circular resonators including baffles. *Chin. J. Phys.* **2021**, *71*, 286–299. [[CrossRef](#)]
34. Rakhshani, M.R. Refractive index sensor based on concentric triple racetrack resonators side-coupled to metal-insulator-metal waveguide for glucose sensing. *J. Opt. Soc. Am. B* **2019**, *36*, 2837–2842. [[CrossRef](#)]
35. Sagor, R.H.; Hassan, M.F.; Sharmin, S.; Adry, T.Z.; Emon, M.R. Numerical investigation of an optimized plasmonic on-chip refractive index sensor for temperature and blood group detection. *Results Phys.* **2020**, *19*, 103611. [[CrossRef](#)]
36. Su, H.; Yan, S.; Yang, X.; Guo, J.; Wang, J.; Hua, E. Sensing features of the Fano resonance in an MIM waveguide coupled with an Elliptical ring resonant cavity. *Appl. Sci.* **2020**, *10*, 5096. [[CrossRef](#)]
37. Zhu, J.; Li, N. MIM waveguide structure consisting of a semicircular resonant cavity coupled with a key-shaped resonant cavity. *Opt. Express* **2020**, *28*, 19978. [[CrossRef](#)] [[PubMed](#)]
38. Chau, Y.-F.C.; Chao, C.-T.C.; Huang, H.; Kumara, N.; Lim, C.; Chiang, H.-P. Ultra-high refractive index sensing structure based on a metal-insulator-metal waveguide-coupled T-shape cavity with metal nanorod defects. *Nanomaterials* **2019**, *9*, 1433. [[CrossRef](#)]
39. Butt, M.A.; Kazanskiy, N.L.; Khonina, S.N. Highly sensitive refractive index sensor based on plasmonic Bow Tie configuration. *Photonic Sens.* **2020**, *10*, 223–232. [[CrossRef](#)]

40. Shi, H.; Yan, S.; Yang, X.; Wu, X.; Wu, W.; Hua, E. A nanosensor based on a metal-insulator-metal bus waveguide with a stub coupled with a racetrack ring resonator. *Micromachines* **2021**, *12*, 495. [[CrossRef](#)]
41. El-Haffar, R.; Farkhsi, A.; Mahboub, O. Optical properties of MIM plasmonic waveguide with an elliptical cavity resonator. *Appl. Phys. A* **2020**, *126*, 486. [[CrossRef](#)]
42. Zhang, Z.; Luo, L.; Xue, C.; Zhang, W.; Yan, S. Fano resonance based on metal-insulator-metal waveguide-coupled double rectangular cavities for plasmonic nanosensors. *Sensors* **2016**, *16*, 642. [[CrossRef](#)] [[PubMed](#)]
43. Binfeng, Y.; Ruohu, Z.; Guohua, H.; Yiping, C. Ultra sharp fano resonances induced by coupling between plasmonic stub and circular cavity resonators. *Plasmonics* **2016**, *11*, 1157–1162. [[CrossRef](#)]
44. Sia, P.D. Overview of Drude-Lorentz type models and their applications. *Nanoscale Syst. Math. Model. Theory Appl.* **2014**, *3*, 1–13.
45. Butt, M.A.; Khonina, S.N.; Kazanskiy, N.L. Plasmonic refractive index sensor based on metal-insulator-metal waveguides with high sensitivity. *J. Mod. Opt.* **2019**, *66*, 1038–1043. [[CrossRef](#)]